



1 Atmospheric oxidation capacity and ozone pollution mechanism in a 2 coastal city of Southeast China: Analysis of a typical photochemical 3 episode by Observation-Based Model

4
5 Taotao Liu^{1,2,3}, Youwei Hong^{1,2}, Mengren Li^{1,2}, Lingling Xu^{1,2}, Jinsheng Chen^{1,2*}, Yahui Bian^{1,2}, Chen Yang^{1,2,3}, Yangbin
6 Dan^{1,2}, Yingnan Zhang⁴, Likun Xue^{4*}, Min Zhao⁴, Zhi Huang⁵, Hong Wang⁶

7
8 ¹Center for Excellence in Regional Atmospheric Environment, Institute of Urban Environment, Chinese Academy of Sciences,
9 Xiamen, China

10 ²Key Lab of Urban Environment and Health, Institute of Urban Environment, Chinese Academy of Sciences, Xiamen, China

11 ³University of Chinese Academy of Sciences, Beijing, China

12 ⁴Environment Research Institute, Shandong University, Jinan, Shandong, China

13 ⁵Xiamen Institute of Environmental Science, Xiamen, China

14 ⁶Fujian Meteorological Science Institute, Fujian Key Laboratory of Severe Weather, Fuzhou, China

15
16 Corresponding authors E-mail: Jinsheng Chen (jschen@iue.ac.cn); Likun Xue (xuelikun@sdu.edu.cn)

17 18 **Abstract:**

19 A typical multi-day ozone (O₃) pollution event was chosen to explore the atmospheric oxidation
20 capacity (AOC), OH reactivity, radical chemistry, and O₃ pollution mechanism in a coastal city of
21 Southeast China, with an Observation-Based Model coupled to the Master Chemical Mechanism (OBM-
22 MCM). The hydroxyl radical (OH) was the predominant oxidant (91±23%) for daytime AOC, while NO₃
23 radical played an important role for AOC during the nighttime (64±11%). Oxygenated volatile organic
24 compounds (OVOCs, 30±8%), NO₂ (29±8%) and CO (25±5%) were the dominant contributors to OH
25 reactivity, accelerating the production of O₃ and recycling of ROx radicals (ROx=OH+HO₂+RO₂).
26 Photolysis of nitrous acid (HONO, 33±14%), O₃ (25±13%), formaldehyde (HCHO, 20±5%), and other
27 OVOCs (17±2%) were the important primary sources of ROx radicals, which played initiation roles in
28 atmospheric oxidation processes. O₃ formation was VOC-sensitive, and controlling emissions of
29 aromatics, alkenes, and long-chain alkanes were benefit for ozone pollution mitigation. Combined with
30 regional transport analysis, the reasons for this O₃ episode were the accumulation of local photochemical
31 production and regional transport. The results of sensitivity analysis showed that VOCs were the limiting
32 factor of radical recycling and O₃ formation, and the 5% reduction of O₃ would be achieved by decreasing
33 20% anthropogenic VOCs. The findings of this study have significant guidance for emission reduction
34 and regional collaboration on future photochemical pollution control in the relatively clean coastal cities
35 of China and similar countries.

36



37 **Keywords:** Atmospheric oxidation capacity; Radical chemistry; O₃ formation mechanism; OH reactivity;
38 OBM-MCM

39

40 **1 Introduction**

41 Tropospheric ozone (O₃) is mainly produced by photochemical reactions of anthropogenic and
42 natural emitted volatile organic compounds (VOCs) and nitrogen oxides (NO_x), and is an important factor
43 resulting in regional air pollution (Zhu et al., 2020; Lu et al., 2018). The elevated O₃ concentrations
44 enhance the atmospheric oxidation capacity (AOC) and have harmful effects on global climate change,
45 ecosystems, and human health (Liu et al., 2019a; Fowler et al., 2009). The formation mechanisms of O₃
46 pollution are extremely difficult to figure out, due to the complex types and sources of its precursors
47 (Simon et al., 2015). O₃ formation is affected by multiple factors such as temporal & spatial distribution,
48 meteorological conditions, atmospheric oxidation processes and regional transport (Gong and Liao, 2019;
49 Chang et al., 2019). To effectively control the tropospheric O₃ pollution, exploration of the photochemical
50 mechanism and judgment on the control factors of O₃ formation become extremely important for
51 scientific community (Chen et al., 2020; Li et al., 2018).

52 The atmospheric oxidation capacity reflects the essential driving force in tropospheric chemistry,
53 and plays an important place in the destruction rates of primary components and production rates of
54 secondary pollutants (Elshorbany et al., 2008). Generally, the AOC levels in the polluted regions are much
55 higher than those at the background sites or remote regions (Geyer et al., 2001; Xue et al., 2016). RO_x
56 radicals, including hydroxyl radical (OH), hydro peroxy radical (HO₂) and organic peroxy radical (RO₂),
57 are very important indicators in atmospheric photochemistry and dominate the atmospheric oxidative
58 capacity (Li et al., 2018). Meanwhile, radical chemistry drives the transformation and recycling of O₃
59 through initiating atmospheric oxidation processes (Wang et al., 2020). Among these radicals, the OH
60 radical accounts for the majority of AOC over 90% during the daytime, thus the OH reactivity (i.e., OH
61 loss) indicates the primary contribution of individual pollutant (Wang et al., 2018a; Mao et al., 2010).
62 Hence, atmospheric oxidation capacity, OH reactivity, and radical chemistry are crucial aspects for
63 understanding the complex atmospheric photochemistry processes (Li et al., 2018). For example, the
64 major primary RO_x sources are the photolysis reaction of O₃, formaldehyde (HCHO), other oxygenated
65 volatile organic compounds (OVOCs), nitrous acid (HONO) and the reactions of O₃ with unsaturated
66 VOCs (Volkamer et al., 2010). The dominant RO_x sources at some rural sites were O₃ photolysis and O₃
67 reactions with VOCs (Li et al., 2018; Martinez et al., 2003), and those at many urban sites were HONO
68 and OVOCs photolysis (Xue et al., 2016; Liu et al., 2012; Emmerson et al., 2005). For oil and gas field



69 sites, there were highly abundant VOCs to promote the formations of O₃, and the contribution of OVOCs
70 photolysis was 2-5 times higher than that in urban areas (Chen et al., 2020; Edwards et al., 2013, 2014).
71 The HONO photolysis was a very important primary ROx source at the high-altitude or background sites.
72 (Acker et al., 2001; Jiang et al., 2020).

73 Current studies of atmospheric O₃ photochemical pollution observations have been conducted at the
74 urban, suburban, rural and remote sites around the world (Smith et al., 2006; Eisele et al., 1997; Kanaya
75 et al., 2001; Hofzumahaus et al., 2009; George et al., 1999; Emmerson et al., 2005; Kanaya et al., 2007;
76 Michoud et al., 2012). In China, O₃ photochemical pollution events have been reported in some megacities,
77 such as Beijing, Shanghai, Guangzhou, and Chengdu (Liu et al., 2012; Tan et al., 2019; Zhu et al., 2020;
78 Wang et al., 2020; Liu et al., 2019b; Ling et al., 2017). Few studies on O₃ photochemical pollution in
79 cities with low O₃ precursor emissions have been reported, and the air quality in these areas usually
80 depends on the change of meteorological conditions. The coastal region of Southeast China is influenced
81 by the East Asian monsoon and acts as an important transport path between the Yangtze River Delta (YRD)
82 and the Pearl River Delta (PRD) (Hu et al., 2019; Liu et al., 2020a; Liu et al., 2020b), which is a good
83 ‘laboratory’ to further explore O₃ photochemical pollution and formation mechanism with relatively low
84 O₃ precursors and complex meteorological conditions (Zhang et al., 2020b; Hu et al., 2020b).

85 The Observation-Based Model (OBM) is widely used to investigate O₃-VOCs-NO_x relationships
86 and radical chemistry (Wang et al., 2018a; Tan et al., 2019). The O₃ sensitivity reveals the non-linear
87 relationship between O₃ and its precursors (i.e., VOCs and NO_x), which was conducted to investigate O₃
88 formation mechanism and control strategies (Wang et al., 2020). The OBM combined with the Master
89 Chemical Mechanism (V3.3.1) (OBM-MCM) has been applied to explore the O₃ photochemical pollution
90 mechanism in different environmental conditions (Chen et al., 2020; Li et al., 2018; Xue et al., 2016;
91 Wang et al., 2018). In this study, we chose a typical multi-day O₃ pollution event in the coastal city Xiamen
92 (Fig. S1). Based on the OBM-MCM analyses, the study aims to clarify (1) the pollution characteristics of
93 O₃ and its precursors, (2) the atmospheric oxidation capacity and radical chemistry, and (3) the O₃
94 formation mechanism and sensitivity analysis. The results are expected to enhance the understanding of
95 O₃ formation mechanism with low O₃ precursor levels, and provide scientific evidence for O₃ pollution
96 control in the coastal cities.

97

98 **2 Materials and methods**

99 **2.1 Study area and field observations**

100 Xiamen is a coastal city in the southeast area of China, to the west coast of the Taiwan Strait. The



101 field campaigns were carried out at the Atmospheric Environment Observation Supersite (24.61° N,
102 118.06° E) on the rooftop of around 70 m high building in the Institute of Urban Environment, Chinese
103 Academy of Sciences. The supersite was equipped with complete monitoring instruments, including gas
104 and aerosol species compositions, O₃ precursors, meteorological parameters, and photolysis rate. Criteria
105 air pollutants of O₃, SO₂, NO-NO₂-NO_x, and CO were monitored by commercial instruments TEI 49i,
106 43i, 42i, and 48i (*Thermo Fisher Scientific, USA*), respectively. The meteorological parameters of wind
107 speed (WS), wind direction (WD), air temperature (T), pressure (P), and relative humidity (RH) were
108 measured by an ultrasonic anemometer (*150WX, Airmar, USA*). HONO was measured with an analyzer
109 for Monitoring Aerosols and Gases in Ambient Air (*MARGA, ADI 2080, Applikon Analytical B.V., the*
110 *Netherlands*). A gas chromatography-mass spectrometer (*GC-FID/MS, TH-300B, Wuhan, CN*) was used
111 for atmospheric VOCs concentrations monitoring, involving about 103 species of VOCs with a 1-hour
112 time resolution. Photolysis frequencies were measured by a photolysis spectrometer (*PFS-100, Focused*
113 *Photonics Inc., Hangzhou, China*). The photolysis rate constants include $J(\text{O}^1\text{D})$, $J(\text{NO}_2)$, $J(\text{H}_2\text{O}_2)$,
114 $J(\text{HONO})$, $J(\text{HCHO})$, and $J(\text{NO}_3)$. Strict quality assurance and quality control were applied, and the
115 detailed descriptions of the monitoring procedures were documented in our previous studies (Zhang et al.,
116 2020b; Wu et al., 2020; Liu et al., 2020a; Liu et al., 2020b; Hu et al., 2020a).

117 2.2 Observation-based chemical box model

118 In this study, the Observation-Based Model (OBM) combined with the latest version 3.3.1 of MCM
119 (MCM v3.3.1; <http://mcm.leeds.ac.uk/MCM/>), involving 142 non-methane VOCs and more than 17000
120 elementary reactions of 6700 primary, secondary and radical species (Jenkin et al., 2003; Saunders et al.,
121 2003), was used to explore the atmospheric oxidation processes and O₃ formation mechanisms. The
122 physical process of deposition within the boundary layer height (BLH), which varied from 300 m during
123 nighttime to 1500 m during the daytime in autumn (Li et al., 2018), was considered in the model.
124 Therefore, the dry deposition velocity was utilized to simulate the deposition loss of some reactants in the
125 atmosphere, which avoided continuous accumulation of pollutant concentrations in the model (Zhang et
126 al., 2003; Xue et al., 2016).

127 The observation data of the gaseous pollutants (i.e., O₃, CO, NO, NO₂, HONO, SO₂, and VOCs),
128 meteorological parameters (i.e., T, P, and RH), and photolysis rate constants ($J(\text{O}^1\text{D})$, $J(\text{NO}_2)$, $J(\text{H}_2\text{O}_2)$,
129 $J(\text{HONO})$, $J(\text{HCHO})$, and $J(\text{NO}_3)$) were input into the OBM-MCM model as constraints. The photolysis
130 rates of other molecules such as OVOCs were parameterized by solar zenith angle and then scaled by the
131 measured $J(\text{NO}_2)$ (Saunders et al., 2003). We pre-ran for 5 days before running the model to initialize the



132 unmeasured compounds and radicals (Xue et al., 2014).

133 OBM-MCM is mainly used to simulate in situ atmospheric photochemical processes and quantify
134 the O₃ production rate, AOC, OH reactivity, and RO_x radical budgets. Among them, primary sources of
135 RO_x, including the photolysis reactions of O₃, HONO, formaldehyde (HCHO), and other OVOCs as well
136 as reactions of VOCs with O₃ and NO₃ radicals, are important (Xue et al., 2016). The termination reactions
137 of RO_x are controlled by cross-reactions with NO_x (under high NO_x conditions) and RO_x (under low
138 NO_x conditions) to form nitric acid, organic nitrates, and peroxides (Liu et al., 2012; Xue et al., 2016).
139 The production rate of O₃ (P(O₃)) includes HO₂+NO and RO₂+NO reactions (Eq. 1), and the destruction
140 of O₃ (D(O₃)) involves reactions of O₃ photolysis, O₃+OH, O₃+HO₂, O₃+VOCs, NO₂+OH, and
141 NO₃+VOCs (Eq. 2). The net O₃ production rate (Pnet(O₃)) is calculated by P(O₃) minus D(O₃) as equation
142 3.

$$143 P(O_3) = k_1[HO_2][NO] + \sum(k_{2i}[RO_2][NO]) \quad (1)$$

$$144 D(O_3) = k_3[O_1D][H_2O] + k_4[O_3][OH] + k_5[O_3][HO_2] + k_6[NO_2][OH] + \\ 145 \sum(k_{7i}[O_3][unsat.VOCs]) + 2 \sum(k_{8i}[NO_3][unsat.VOCs]) \quad (2)$$

$$146 Pnet(O_3) = P(O_3) - D(O_3) \quad (3)$$

147 where k_i is the related reaction rate constant. Detailed descriptions of the chemistry calculation can be
148 found elsewhere (Chen et al., 2020; Wang et al., 2018a; Xue et al., 2014).

149 Relative incremental reactivity (RIR), an index to diagnose the sensitivity of O₃ formation to
150 precursors, is defined as the ratio of the differences in O₃ production rate to the difference in precursor
151 concentrations (Chen et al., 2020). Here, the $\Delta X/X$ in the OBM-MCM represents the percentage reduction
152 in the input concentrations of each targeted O₃ precursor group and this value is adopted as 20% (Liu et
153 al., 2020c).

$$154 RIR = \frac{\Delta P(O_3)/P(O_3)}{\Delta X/X} \quad (4)$$

155

156 2.3 Meteorological data and back trajectory calculation

157 The backward trajectories of air masses arriving at the observation site were calculated by the
158 MeteoInfo during the episode (Wang et al., 2014). The backward trajectories with 72-h were run with the
159 time resolution of 3 hours at 100 m height above ground level, and starting time was 0:00 LT and the
160 ending time was 23:00 LT. Meteorological data were provided by NOAA ARL
161 (<ftp://arlftp.arlhq.noaa.gov/pub/archives/gdas1>). The Final Operational Global Analysis data (FNL) is

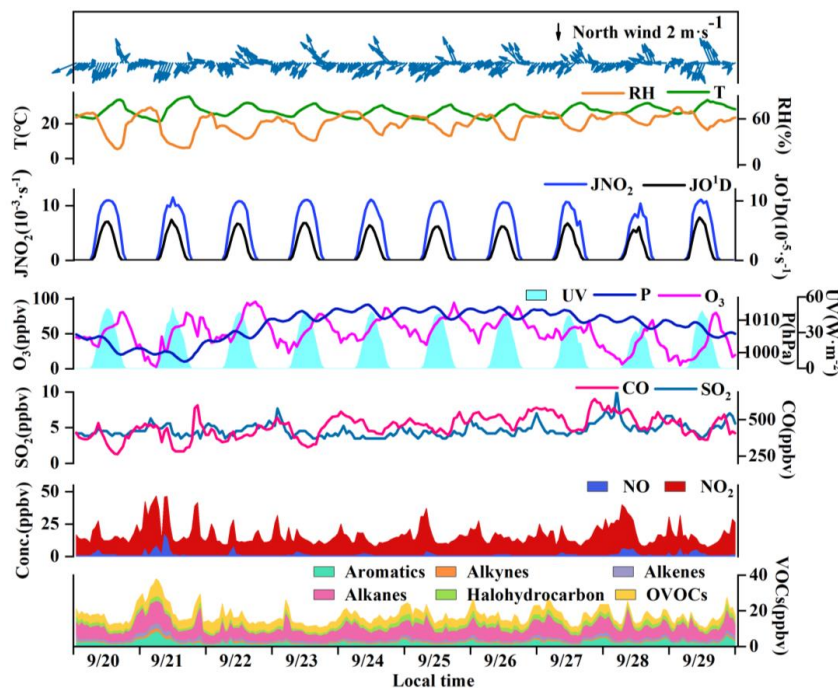


162 from the Global Data Assimilation System and analyzes results with the model which is also used by the
163 National Center for Environmental Prediction (NCEP) in the Global Forecast System (GFS)
164 (<https://rda.ucar.edu/datasets/ds083.2/>). The weather charts were conducted using Grid Analysis and
165 Display System (GrADS) with the specific programmed script files. A detailed description of the synoptic
166 information was shown in our previous study (Wu et al., 2019).

167 **3 Results and discussion**

168 **3.1 Overview of observations**

169 The O₃ pollution events frequently appeared in the coastal city Xiamen during autumn time, related
170 to the West Pacific Subtropical High (WPSH), carrying high temperature, low RH, and stagnant weather
171 conditions, encouraging the formation and accumulation of O₃ in the southeast coastal area (Wang et al.,
172 2018a). The daily maximum 8-h-average O₃ concentrations (MDA8h O₃) from 20 to 29 Sep, 2019 ranged
173 from 53 to 85 ppbv, partly exceeding the Grade II of China's National Ambient Air Quality Standard of
174 75 ppbv. The time series and descriptive statistics of air pollutants and meteorological parameters during
175 this multi-day O₃ pollution event are shown in Fig. 1 and Table 1. During this period, the dominant wind
176 direction was northeast, with an average wind speed of $1.8 \pm 0.9 \text{ m}\cdot\text{s}^{-1}$. The maximum hourly temperature
177 was as high as 35 °C, and the average RH was $56.4 \pm 12.6\%$. Solar radiation intensity and J(NO₂) were
178 strong, compared to those of the Yellow River Delta (Chen et al., 2020), Shanghai (Zhu et al., 2020) and
179 Hong Kong (Xue et al., 2016). In general, these meteorological parameters were conducive to the
180 production and accumulation of O₃. In addition, O₃ concentrations at nighttime kept relatively high (Fig. 1),
181 indicating the influence of regional transport and little NO titration (Zhang et al., 2020a; Wu et al., 2020).
182 Figure S2 shows the 72 h back trajectories at the monitoring site. Among them, 80% of the air masses
183 came from the Yellow Sea, and the other 20% air masses originated from the northeast China through
184 long-range transport.



185

186 **Figure 1.** Time series of major trace gases, photolysis rate constants, and meteorological parameters during 20-
 187 29 Sep. 2019 in Xiamen.

188

189 **Table 1.** Descriptive statistics of major trace gases (ppbv) and meteorological parameters during 20-29 Sep. 2019

| Parameters | Mean±SD | Median | Max |
|---------------------------------|-----------|--------|------|
| MDA8h O ₃ | 67.4±17.2 | 52.6 | 89.3 |
| TVOCs | 17.2±4.8 | 16.1 | 38.0 |
| CO | 452±77.3 | 454 | 641 |
| NO | 1.4±1.3 | 0.8 | 17.1 |
| NO ₂ | 15.4±6.9 | 13.6 | 40.9 |
| SO ₂ | 4.7±0.9 | 4.6 | 10.2 |
| T (°C) | 27.3±3.21 | 26.9 | 35.6 |
| RH (%) | 56.4±12.6 | 56.6 | 75.0 |
| P (hPa) | 1008±4.57 | 1010 | 1015 |
| UV (W·m ⁻²) | 46.4±1.12 | 0 | 51.1 |
| Wind speed (m·s ⁻¹) | 1.8±0.9 | 1.6 | 3.8 |
| Wind direction (°) | 90.8±90.4 | 45.0 | 337 |

190

Table 2. Measured VOCs concentrations during 20-29 Sep. 2019 in Xiamen (Units: pptv)

| Chemicals | Mean±SD | Chemicals | Mean±SD |
|------------------------|------------------|----------------|------------------|
| Aromatics | 2131±1236 | Alkanes | 6970±2325 |
| toluene | 995±632 | ethane | 1552±342 |
| m/p-xylene | 392±326 | propane | 1546±608 |
| benzene | 236±95 | iso-pentane | 930±316 |
| o-xylene | 154±121 | n-butane | 844±365 |
| ethylbenzene | 138±94 | n-dodecane | 618±101 |
| styrene | 76±65 | iso-butane | 494±201 |
| 1,2,4-trimethylbenzene | 75±37 | n-pentane | 254±157 |



| | | | |
|---------------------------|------------------|--------------------|-----------------|
| m-ethyltoluene | 16±11 | n-hexane | 134±184 |
| p-ethyltoluene | 10±6 | 3-methylhexane | 116±93 |
| iso-propylbenzene | 5±3 | n-heptane | 104±78 |
| 1,3,5-trimethylbenzene | 8±6 | 3-methylpentane | 82±48 |
| o-ethyltoluene | 8±5 | 2-methylhexane | 67±38 |
| 1,2,3-trimethylbenzene | 7±5 | 2-methylpentane | 56±46 |
| n-propylbenzene | 7±4 | 2,3-dimethylbutane | 54±33 |
| Halocarbons | 1951±572 | cyclohexane | 42±15 |
| dichloromethane | 998±392 | n-undecane | 33±35 |
| 1,2-dichloroethane | 499±210 | n-octane | 24±15 |
| chloromethane | 294±75 | n-nonane | 15±13 |
| 1,2-dichloropropane | 88±34 | 2,2-dimethylbutane | 15±7 |
| bromomethane | 47±23 | n-decane | 14±11 |
| trichloroethene | 15±6 | Alkenes | 1205±464 |
| 1,4-dichlorobenzene | 9±3 | ethene | 671±361 |
| OVOCs | 4246±1263 | propene | 207±116 |
| acetone | 2802±750 | isoprene | 171±232 |
| 2-butanone | 799±430 | trans-2-pentene | 105±62 |
| 2-propanol | 343±283 | 1-butene | 16±21 |
| 2-methoxy-2-methylpropane | 169±97 | cis-2-butene | 12±12 |
| acrolein | 66±22 | 1-pentene | 10±7 |
| 4-methyl-2-pentanone | 16±15 | 1,3-butadiene | 8±7 |
| 2-hexanone | 12±3 | trans-2-butene | 4±4 |
| | | Acetylene | 674±290 |

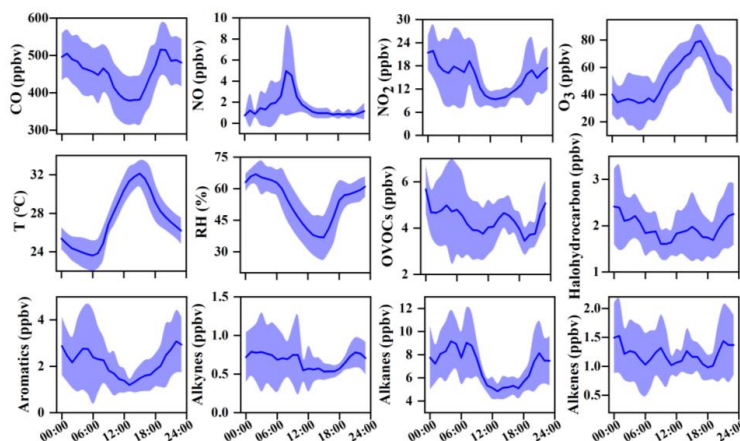
191

192 Table 2 lists the detailed VOCs concentrations during the observation period. Alkanes (6970±2325
 193 pptv) were the predominant components of total VOCs, followed by OVOCs (4246±1263 pptv),
 194 aromatics (2131±1236 pptv), halocarbons (1951±572 pptv), alkenes (1205±464 pptv), and acetylene
 195 (674±290 pptv). The ratio of ethene/ethane (0.4±0.2) was significantly ($p < 0.05$) lower than that in Hong
 196 Kong (0.7±0.1) with significant aged air masses, indicating that the high O₃ in Xiamen might be partially
 197 attributed to the aged air masses (e.g., transport of air from polluted regions or intense atmospheric
 198 oxidation) (Wang et al., 2018a). The concentration of TVOCs in Xiamen (17.2±4.8 ppbv) was much lower
 199 than that in the developed areas with large anthropogenic emissions (i.e., Beijing (65.6 ppbv), Hangzhou
 200 (55.9 ppbv), Guangzhou (47.3 ppbv), Nanjing (43.5 ppbv), Hong Kong (26.9 ppbv) and Shanghai (29.7
 201 ppbv), but was higher than that at the background site (i.e., Mt. Wuyi, 6.1 ppbv) (Li et al., 2019; Hong et
 202 al., 2019). Figure S3 shows the contributions of top 10 VOCs species (including alkenes and aromatics)
 203 to the total ozone formation potential (OFP), which was calculated by the localized maximum incremental
 204 reactivity in China (Zhang et al., 2021). The key VOCs species with the highest OFP was ethene (3.6±2.0
 205 $\mu\text{g}\cdot\text{m}^{-3}$), m/p-xylene (2.2±1.9 $\mu\text{g}\cdot\text{m}^{-3}$), toluene (2.2±1.5 $\mu\text{g}\cdot\text{m}^{-3}$), propene (1.3±0.8 $\mu\text{g}\cdot\text{m}^{-3}$) and isoprene
 206 (1.3±1.7 $\mu\text{g}\cdot\text{m}^{-3}$).

207 The O₃ formation process depends on its precursors and related environmental conditions, while the



208 photochemical reactions during the daytime are the basis for O₃ changes. Figure 2 shows the diurnal
209 patterns of major trace gases and meteorological parameters during 20-29 Sep. 2019. The O₃
210 concentration maintained at relatively low levels from night to 07:00 LT, then rose and reached its
211 maximum at around 17:00 LT. O₃ peak in the afternoon was related to the accumulation of both local
212 photochemical reaction and potential regional transport (including O₃ and its precursors in the upwind
213 direction to the observation site), and the detailed analysis will be shown in Section 3.3.2. The reduction
214 of observed O₃ (Δ O₃) in the early morning rush hour caused by NO titration did not appear, verifying the
215 impacts of regional transport (Liu et al., 2019b; Zeren et al., 2019; Chen et al., 2020). The diurnal patterns
216 of VOCs and NO_x were similar, with the highest concentrations at around 08:00 LT and then decreasing
217 during 9:00~16:00 LT and increasing at night, which is related to the human activities emissions
218 (including vehicle exhaust and industry emission), photochemical reaction and the variations of boundary
219 layer (Elshorbany et al., 2008; Hu et al., 2020b).



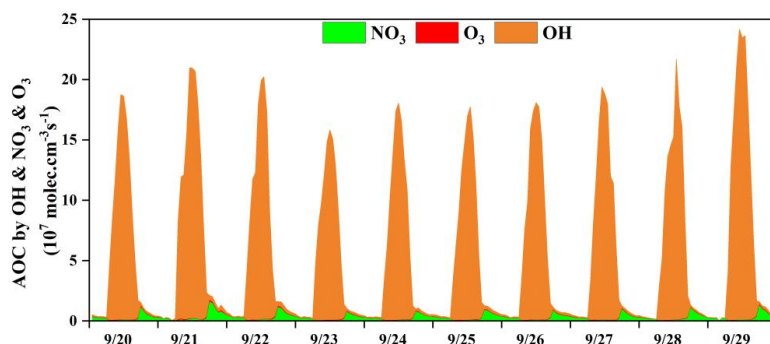
220

221 **Figure 2.** Average diurnal patterns of major trace gases and meteorological parameters during 20-29 Sep. 2019 in
222 Xiamen. The error bar is the standard error.

223

224 3.2 Atmospheric oxidation and radical chemistry

225 3.2.1 Atmospheric oxidation capacity (AOC)



226

227 **Figure 3. Time series of the model-calculated Atmospheric Oxidation Capacity (AOC) in Xiamen during 20-29**
228 **Sep. 2019.**

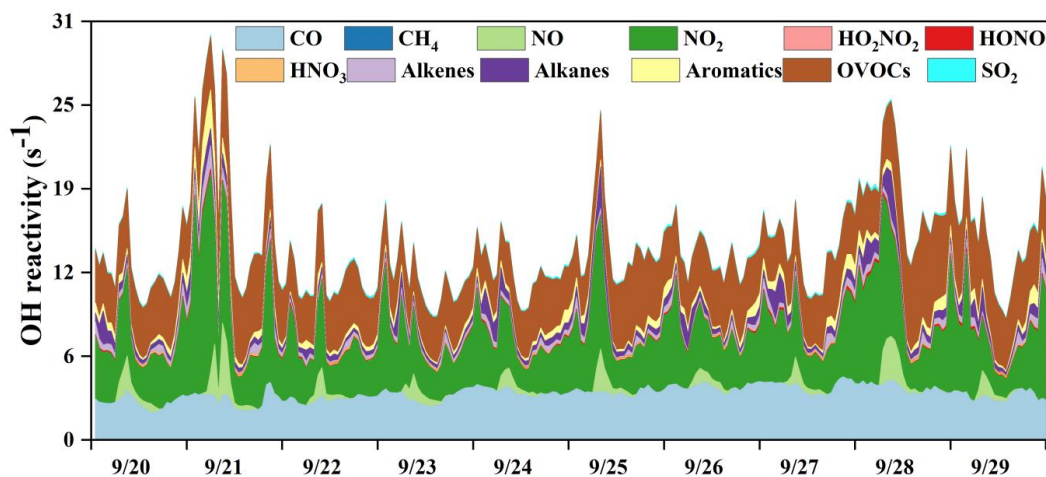
229 Figure 3 shows the time series of the model-calculated AOC during the O₃ pollution period. The
230 AOC determines the removal rate of primary pollutants and the production rate of secondary pollutants,
231 and was the basis for reflecting atmospheric photochemical pollution (Geyer et al., 2001). AOC is
232 calculated as the sum of oxidation rates of various primary pollutants (CO, NO_x, VOCs, etc.) by the major
233 oxidants (i.e., OH, O₃, NO₃) (Chen et al., 2020; Xue et al., 2016; Xue et al., 2014). In this study, the
234 average daytime AOC was 10.0×10^7 molecules $\text{cm}^{-3} \text{s}^{-1}$, which was comparable to Hong Kong (6.3×10^7
235 molecules $\text{cm}^{-3} \text{s}^{-1}$), higher than those in Shanghai (3.5×10^7 molecules $\text{cm}^{-3} \text{s}^{-1}$) and a rural site of Berlin
236 (1.4×10^7 molecules $\text{cm}^{-3} \text{s}^{-1}$), but lower than that in Santiago (3.2×10^8 molecules $\text{cm}^{-3} \text{s}^{-1}$) (Li et al.,
237 2018; Chen et al., 2020; Xue et al., 2016; Geyer et al., 2001; Zhu et al., 2020). The results of AOC
238 characteristics in different regions were decided by the precursor concentrations/types and photochemical
239 environment.

240 According to the diurnal patterns of the AOC contributed by OH, O₃, and NO₃, the predominant
241 oxidant was OH ($91 \pm 23\%$) during the daytime, followed by NO₃ ($8 \pm 20\%$) and O₃ ($1 \pm 2\%$). Meanwhile,
242 the diurnal characteristics of AOC were consistent with the profile of the model-calculated OH (Fig. S4)
243 and the observed photolysis rate constants (Fig.1) (Zhu et al., 2020). Meanwhile, NO₃ ($64 \pm 11\%$) played
244 the most important role in the oxidant capability during the nighttime, followed by OH ($29 \pm 12\%$) and O₃
245 ($6 \pm 1\%$). In particular, the contribution of NO₃ to AOC reached the maximum of 80% at around 18:00 LT,
246 when the concentrations of O₃ and NO₂ were relatively high and accelerated the formation of NO₃ (Fig.2).
247 In addition, solar radiation was woken during the nighttime, which resulted in the accumulation of NO₃
248 due to the cease of photolysis of NO₃ (Rollins et al., 2012; Chen et al., 2020). AOC contributed by O₃
249 was negligible, owing to the relatively low concentration of alkenes at the monitoring site (Fig.1 and
250 Table 2), since O₃ contributed to the oxidation capacity through alkenes ozonolysis (Xue et al., 2016). In



251 summary, the OH radical dominated the AOC in Xiamen, and it was necessary to further explore the
252 partitioning of OH reactivity among different precursor groups.

253

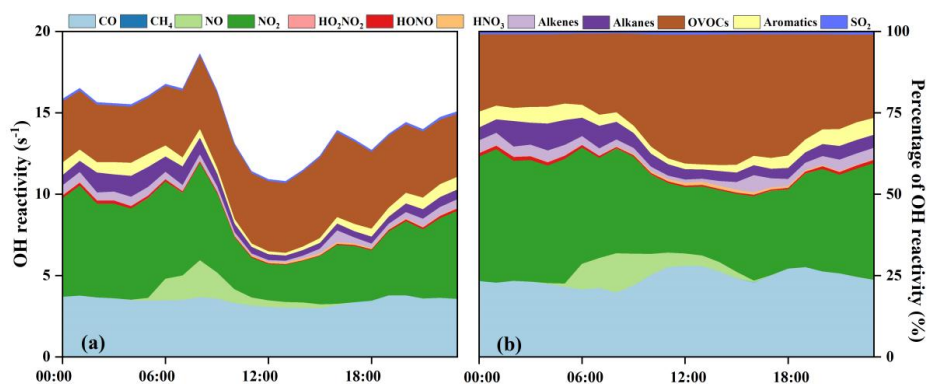


254

255 **Figure 4. Time series of model-calculated OH reactivity and its partitioning to the major reactants in Xiamen**
256 **during 20-29 Sep. 2019.**

257

258



259

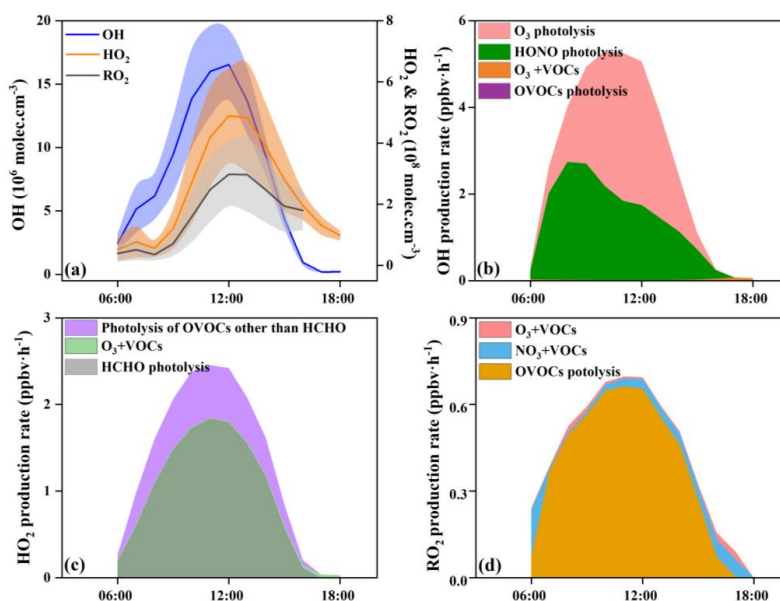
260 **Figure 5. (a) Diurnal patterns and (b) percentage of model-calculated OH reactivity and its partitioning to the**
261 **major reactants**

262 The OH reactivity is an indicator for the OH chemical loss frequency, computed as the reaction rates
263 of OH with CO, NO_x, SO₂, HONO, HNO₃, HO₂NO₂, and VOCs (Whalley et al., 2016; Chen et al., 2020).
264 Zhu et al. (2020) found that unmeasured species and unknown secondary products contributed
265 considerably to the actual OH reactivity. Time series and diurnal patterns of model-calculated OH
266 reactivity as well as its partitioning to the major reactants during the episode are shown in Fig. 4 and Fig.



267 5. The OH reactivity reached the peak ($18.6 \pm 4.8 \text{ s}^{-1}$) at around 8:00 LT, mainly caused by the reaction of
268 OH with NO_x, since vehicle exhaust emitted large amounts of NO_x during rush hours. The average daily
269 OH reactivity was $14.4 \pm 3.83 \text{ s}^{-1}$, which was much lower than those in some polluted regions in Santiago
270 (42 s^{-1}) and the PRD (50 s^{-1}), comparable to that at a rural site in Nashville (11 s^{-1}), but higher than that
271 at a mountain site in Pennsylvania (6 s^{-1}) (Elshorbany et al., 2008; Lou et al., 2010a; Lou et al., 2010b;
272 Kovacs et al., 2003; Ren et al., 2005). Figure 5 shows the diurnal variations and percentage of model-
273 calculated OH reactivity to the major reactants during the episode. As shown in Fig. 5b, OVOCs ($30 \pm 8 \%$)
274 and NO₂ ($29 \pm 8\%$) were the dominant contributors to OH reactivity, followed by CO ($25 \pm 5\%$), alkanes
275 ($5 \pm 3\%$), aromatics ($3 \pm 2\%$), alkenes ($3 \pm 1\%$), and NO ($2 \pm 4\%$). The partitioning of OH reactivity elucidated
276 the inherent photochemical processes and major reactants in Southeast China. High OH reactivity of
277 OVOCs, NO₂, and CO would promote the production of RO_x radical. Therefore, the investigation of
278 detailed chemical budget of the RO_x, recycling, and termination reaction is meaningful to figure out the
279 complex atmospheric photochemistry (Li et al., 2018; Lou et al., 2010b).

280 3.2.2 Radical chemistry



281
282 **Figure 6. Model-simulated daytime average diurnal variations in (a) OH, HO₂, and RO₂ concentrations, and**
283 **average primary production rates of (b) OH, (c) HO₂, and (d) RO₂ during 20-29 Sep. 2019 in Xiamen.**

284 With the influence of NO_x and VOCs, OH, HO₂, and RO₂ undergo efficient recycling and produce
285 secondary pollutants, such as O₃ and OVOCs (Sheehy et al., 2010). Figure 6 shows the model-simulated
286 OH, HO₂, and RO₂ concentrations and their primary sources. The detailed time series of RO_x



287 concentrations and chemical budget are summarized in Fig. S4. Figure 6a shows the diurnal variations of
288 the simulated OH, HO₂, and RO₂. The maximum daily values of OH, HO₂, and RO₂ concentrations were
289 2.4×10^7 , 7.9×10^8 and 4.7×10^8 molecules cm⁻³, with the daytime average concentrations of 7.4×10^6 ,
290 2.4×10^8 and 1.7×10^8 molecules cm⁻³, respectively. Model-predicted concentrations of OH in Xiamen
291 were higher than that in the the Yellow River Delta (an oil field with high VOCs emission), while the
292 concentrations of HO₂ and RO₂ showed a reverse trend (Chen et al., 2020). The RO_x recycling of
293 OH→RO₂ was mainly controlled by the reaction of OH+VOCs, and the RO₂→HO₂ and HO₂→OH
294 depended on the reactions with NO (Fig.7). Combined with the ratio of VOCs/NO_x (1.1 ± 0.4), it was
295 convinced that NO_x would not be the limiting factor in the radical recycling processes. Hence, efficient
296 conversions of radical propagation of RO₂+NO→HO₂ and HO₂+NO→HO were expected, and
297 OH+VOCs→RO₂ reaction was the rate-depended step of the radical recycling in our study. The detailed
298 radical chemistry would be further discussed as follows.

299 Figure 6b shows the daytime average diurnal variations of primary OH sources. HONO photolysis
300 reached the maximum of 2.7 ppb h^{-1} at around 8:00 LT, which occupied $56 \pm 19\%$ of the total OH primary
301 production rates. The second source of OH primary production was O₃ photolysis ($42 \pm 21\%$), and the
302 percentages of O₃+VOCs and OVOCs photolysis were minor. The highest HONO photolysis rate
303 appeared in the morning rush hour, suggesting the influence from vehicle emissions and nocturnal
304 accumulation of HONO (Hu et al., 2020a). Considering the recycling of radicals, the reaction of HO₂+NO
305 ($8.0 \pm 6.2 \text{ ppb h}^{-1}$) dominated the total production of OH (Fig. S4a). Meanwhile, OH-initiated oxidations
306 of VOCs ($4.9 \pm 3.3 \text{ ppb h}^{-1}$) consumed OH most during the daytime, followed by OH+CO ($2.6 \pm 1.9 \text{ ppb}$
307 h^{-1}), OH+NO₂ ($2.4 \pm 1.1 \text{ ppb h}^{-1}$), OH+NO ($0.6 \pm 0.3 \text{ ppb h}^{-1}$), and OH+O₃ ($0.2 \pm 0.1 \text{ ppb h}^{-1}$).

308 In this study, HCHO photolysis was identified as the most important source for HO₂ primary
309 formation, with an average production rate of $1.1 \pm 0.6 \text{ ppb h}^{-1}$ (Fig.6c), followed by the other OVOCs
310 photolysis ($0.4 \pm 0.2 \text{ ppb h}^{-1}$). The rate of OVOCs photolysis in Xiamen was much lower than that in some
311 megacities, such as Beijing (Liu et al., 2012) and Hong Kong (Xue et al., 2016). The reaction of OH+CO
312 ($2.6 \pm 2.2 \text{ ppb h}^{-1}$) and RO₂+NO ($2.5 \pm 1.5 \text{ ppb h}^{-1}$) were also important sources of HO₂ (Fig. S4b). The
313 main sinks of HO₂ were HO₂+NO ($7.9 \pm 6.2 \text{ ppb h}^{-1}$), while HO₂+HO₂ and HO₂+RO₂ were negligible.

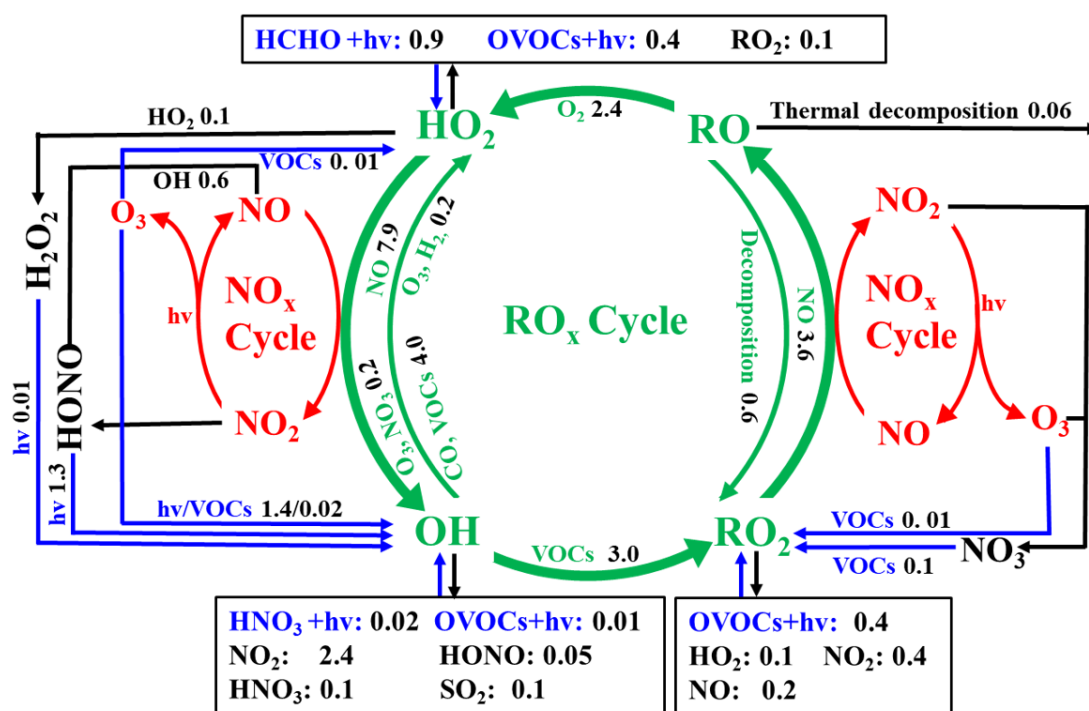
314 In Fig. 6d, OVOCs photolysis contributed most to primary RO₂ production with a rate of 0.5 ± 0.2
315 ppb h^{-1} , accounting for $85 \pm 20\%$ of total RO₂ primary production. The reactions of unsaturated VOCs and
316 NO₃ were the second important source, accounting for $11 \pm 18 \%$ of the total primary RO₂. The radical



317 recycling rate of OH+VOCs was 8.4 times higher than the sum of RO₂ primary production. The
 318 consumption reaction of RO₂ was mainly caused by RO₂+NO (3.7±2.9 ppb h⁻¹), and the cross-reactions
 319 by RO_x themselves were limited.

320 The daytime average RO_x budget and its recycling were also demonstrated (Fig. 7). For the RO_x
 321 primary sources, the photolysis of HONO (33±14%), O₃ (25±13%), HCHO (20±5%) and other OVOCs
 322 (17±2%) were the major contributors. For RO_x recycling, CO and VOCs reacted with OH producing HO₂
 323 and RO₂ with the average rate of 4.0 and 4.4 ppbv h⁻¹, respectively. RO₂+NO and HO₂+NO enhanced the
 324 production of RO (3.6 ppbv h⁻¹) and OH (7.9 ppbv h⁻¹), with O₃ formed as a by-product. For the
 325 termination processes, the reactions of RO_x with NO_x were approximately 2-5 times faster than the cross-
 326 reactions of RO_x.

327



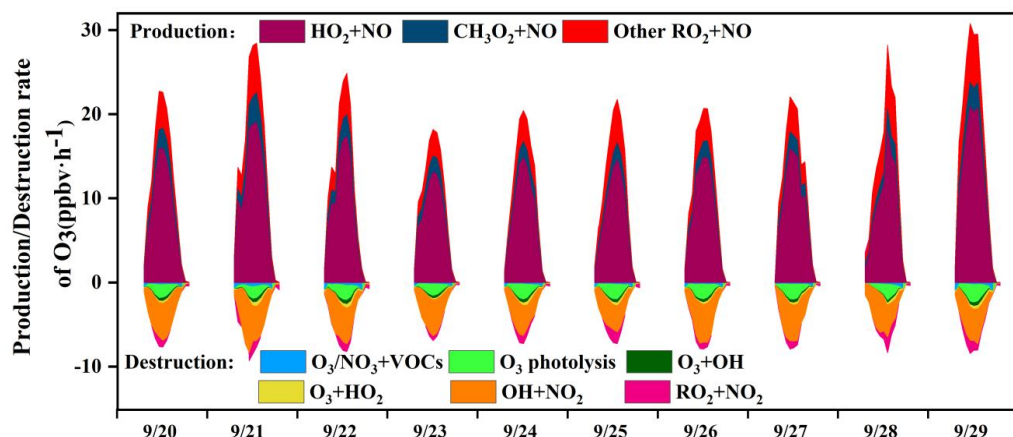
328

329 **Figure 7.** Daytime RO_x budget during 20-29 Sep. 2019 in Xiamen. The unit is parts per billion per hour. The blue,
 330 black, and green lines and words indicate the production, destruction, recycling pathways of radicals, respectively.

331 3.3 O₃ formation mechanism

332 3.3.1 Chemical budget and sensitivity analysis of O₃ production

333



334

335

Figure 8. Time series of model-simulated O₃ chemical budgets during 20-29 Sep. 2019 in Xiamen.

336

337

338

339

340

341

342

343

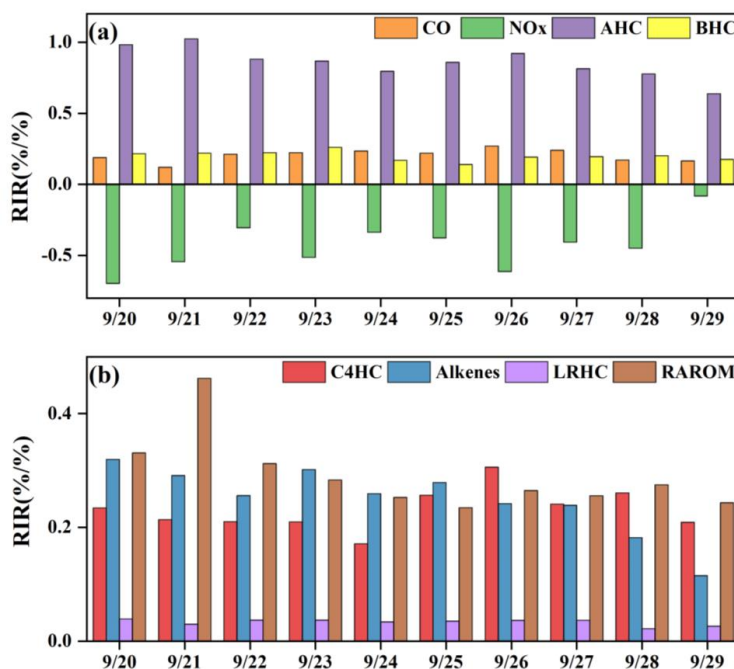
344

345

346

347

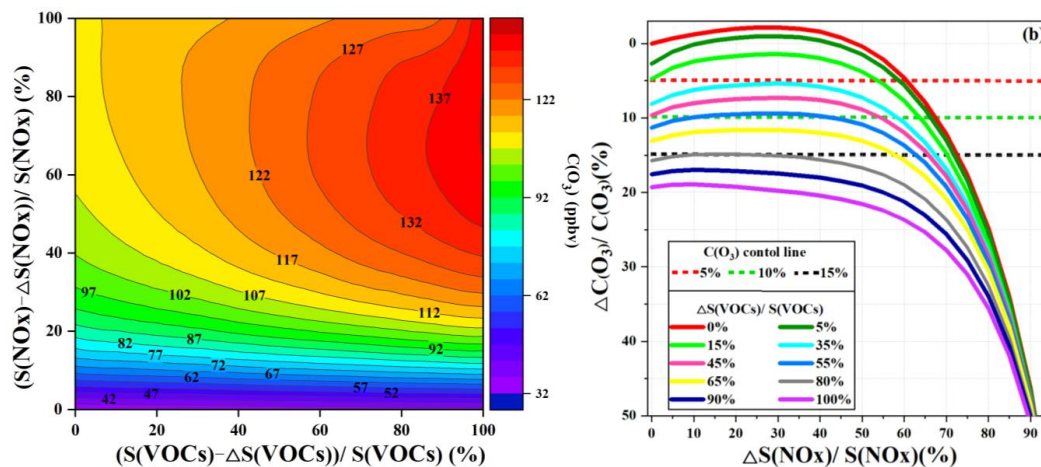
The in situ O₃ production mechanism was examined, and the detailed reaction weights are shown in Fig. 8. The daytime rate of HO₂+NO was 7.9±6.2 ppb h⁻¹, accounting for 68±4% of the total O₃ production. This result was consistent with that in section 3.2.2. The OH radical was the initiator of photochemical O₃ formation, and the main sources of OH from HO₂+NO was also the dominant pathway to produce O₃ (Liu et al., 2020c). The second pathway of O₃ production was RO₂+NO (3.6±2.0 ppb h⁻¹). The reaction of RO₂+NO contained more than 1000 types of RO₂ radicals, and the pathway of CH₃O₂+NO (34±6%) contributed the most among them. In contrast, the contributors of O₃ destruction were OH+NO₂ (61±18%), followed by O₃ photolysis (18±9%), RO₂+NO₂ (9±10%), O₃+HO₂ (4±4%), and O₃+OH (4±2%), while the other pathways of O₃+VOCs as well as NO₃+VOCs, contributed limitedly. In addition, the net O₃ production (9.1±5.7 ppb h⁻¹) in Xiamen was ~2-5 times lower than that derived from the metropolis of Shanghai (26 ppb h⁻¹), Lanzhou (23 ppb h⁻¹) and Guangzhou (50 ppb h⁻¹), reflecting the influence of O₃ precursors emissions and photochemical conditions (Xue et al., 2014).



348

349 **Figure 9. The model-calculated RIRs for (a) major O₃ precursor groups and (b) the AHC sub-groups during high**
350 **O₃ daytime (06:00-18:00 LT) (AHC: anthropogenic hydrocarbons; BHC: biogenic hydrocarbons; RAROM:**
351 **aromatics except for benzene; LRHC: low reactivity hydrocarbons; C4HC: alkenes, and alkanes with ≥4 carbons).**

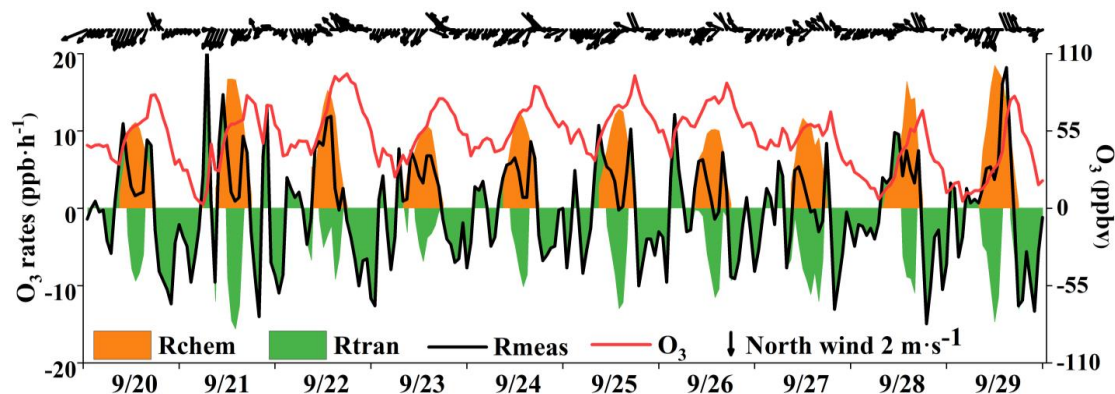
352 In this study, we also calculated the relative incremental reactivity (RIR) to diagnose the sensitivity
353 of O₃ formation to its precursors. Figure 9 shows the RIR values for major groups of O₃ precursors.
354 Around 50 types of VOCs were classified as anthropogenic hydrocarbons (AHC), and the isoprene was
355 categorized into biogenic hydrocarbons (BHC), with AHC further divided into four groups of reactive
356 aromatics (RAROM, including aromatics except for benzene), low reactivity hydrocarbons (LRHC,
357 including methane, ethane, acetylene, propane, and benzene), alkenes, and alkanes with ≥4 carbons
358 (C4HC). The in situ O₃ production was highly VOCs-sensitive, especially for AHC-sensitive
359 (0.63–1.02 %/%) (Fig. 9a), followed by CO (0.17–0.27 %/%) and BHC (0.14–0.26 %/%), indicating the
360 impacts from anthropogenic activities and flourishing vegetation emissions (Liu et al., 2020a; Lin et al.,
361 2020). The RIRs were NO_x-negative ranging from -0.70 to -0.08. As shown in Fig. 9b, the contributors
362 of AHC sub-groups to RIRs were RAROM (0.24–0.46 %/%), C4HC (0.17–0.30 %/%), alkenes
363 (0.11–0.32 %/%), and LRHC (0.03–0.04 %/%). Therefore, the reduction of aromatics, alkenes, and longer
364 alkanes effectively decreased O₃ production, and the reduction of NO_x might aggravate O₃ pollution.



365
366 **Figure 10 (a) Isoleth diagrams of modeled O₃ production potential (C(O₃)) on S(VOCs) and S(NOx) remaining**
367 **percentages (i.e., (S(VOCs)-ΔS(VOCs))/S(VOCs)) and (S(NOx)-ΔS(NOx))/S(NOx)); (b) Relationship of C(O₃)**
368 **increment percentage (ΔC(O₃)/C(O₃)) with S(NOx) and S(VOCs) reduction percentages (ΔS(NOx)/S(NOx) and**
369 **ΔS(VOCs)/S(VOCs)). Note: C(O₃), S(NOx), and S(NOx) represent the concentrations of corresponding**
370 **pollutants.**

371 In order to investigate the O₃ control strategies in the relatively clean coastal city, the scenario
372 analysis with reduction by 0-100% at intervals of 5% for the reduction of anthropogenic VOCs
373 (ΔS(VOCs)/S(VOCs) and NOx (ΔS(NOx)/S(NOx)) were conducted using the OBM-MCM. According
374 to the Empirical Kinetic Modeling Approach (EKMA) and scenario analysis, O₃ formation was in the
375 NO-titration regime (Fig. 10), in accordance with those of RIR analysis. The maximum value of MDA8h
376 O₃ during the monitoring period was 85 ppbv, exceeding the national air quality standard of 75 ppbv for
377 O₃ by 13%. Hence, the O₃ reductions of 5%, 10%, and 15% were set to discuss the reduction schemes of
378 anthropogenic VOCs and NOx. As shown in Fig. 10b, achieving the 5% control target were 1) S(VOCs)
379 is reduced by 15%, while S(NOx) remains unchanged; 2) S(VOCs) is reduced larger than 35%; 3) S(NOx)
380 reduction is higher than 60%. In addition, the 10% of O₃ control target was achieved by the 45% reduction
381 of S(VOCs), and the S(NOx) keeps original emission. In view of the long-term control strategy of NOx
382 and VOCs, S(VOCs) reduced by 55% and 80% could decrease 10% and 15% O₃ concentrations,
383 respectively. Although VOCs and NOx control measures were drastically implemented, it is still
384 challenging to achieve the 15% O₃ control goals in urban areas with relatively low precursor emissions.
385 Meanwhile, as the O₃ sensitivity changed under the implementation of control measures, it is necessary
386 to adjust timely the reduction of VOC and NOx policies.

387 3.3.2 O₃ from local photochemical production and regional transport



388

389

390

391

Figure 11. O₃ accumulation and contributions from local photochemical production and regional transport, and Rchem, Rtran, and Rmeas in figure caption represent local O₃ photochemical production, regional transport and observed O₃ formation rate, respectively.

392

393

394

395

396

397

398

399

400

401

Previous studies have found that the variation of O₃ mixing ratios was mainly influenced by chemical and physical processes (Xue et al., 2014; Tan et al., 2018). Figure 11 shows the time series of O₃ accumulation and contributions from local photochemical production and regional transport. The observed rate of change in O₃ (Rmeas) was calculated by the derivative of the observed O₃ concentrations (Rmeas=d(O₃)/dt). The local O₃ production (Rchem) was calculated by Equation 3, and computed hourly by the OBM as described in Section 2.2. The regional transport (Rtran) was calculated by the equation of Rtran=Rmeas–Rchem, including horizontal and/or vertical transport, deposition and so on. The positive values of Rtran represented the O₃ import of regional transport, while the negative values indicated the O₃ export and deposition. We quantified the contributions of local photochemical formation and regional transport to the observed O₃, and figured out the reasons for the O₃ pollution process.

402

403

404

405

406

407

408

409

410

411

412

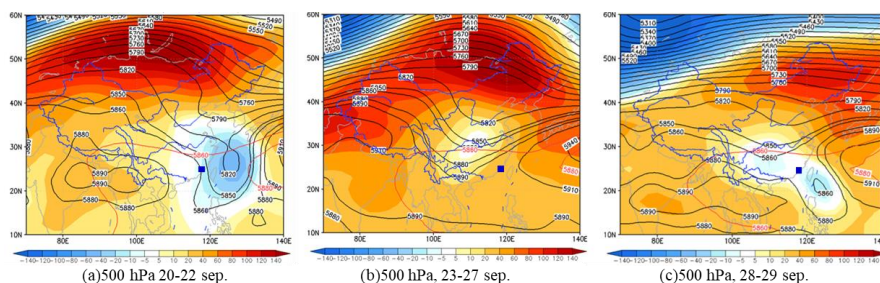
As shown in Fig. 11, two regular O₃ import phenomenon with positive values of Rtran were observed, and the curve of the Rmeas showed the “M” trend during the daytime. The first transient intense O₃ import happened in the early morning, which was mainly attributed to the residual ozone from the day before. The O₃ export was remarkable at around 10:00-15:00, indicating the potential impacts on air quality in downwind areas. When the near-surface wind direction changed from northeast to southeast, the second O₃ import phenomenon occurred in the afternoon (16:00-19:00 LT) in four days (20, 25 27 and 29 Sep.). Due to the Rtran in the afternoon, the daily maximum O₃ values appeared at around 17:00 LT. However, the maximum daily value of O₃ at this observation site generally appeared at around 15:00 LT without regional transport (Wu et al., 2019). Under the conditions of southeast wind direction, downtown area with high density vehicles would make O₃ and its precursors transmitting to our observation site, consistent with the diurnal patterns of NO₂, OVOCs, alkanes, and aromatic in the early morning and



413 afternoon (Fig. 2) to match with the “M” trend of R_{meas} . This result indicated that the sudden changes
414 of near-surface winds corresponding to the variation in the transport of the urban plume.

415 According to photochemical parameters including UV, JNO_2 , JO^1D and the synoptic situations (Fig.
416 1, Fig. S5 and Fig.12), the environmental conditions also favored the O_3 pollution process during the
417 observation periods. The contribution of R_{chem} (daily maximum: ranged from 10.2 to 19.1 $ppb\ h^{-1}$)
418 during the daytime was observed (Fig.11). In Fig. S5abc, the monitoring site was continuously affected
419 by the northerly O_3 polluted airflow from YRD, due to the typhoon ‘Tapah’ from 20 to 22 Sep. 2019. The
420 transport of O_3 import appeared on 21 Sep. ($7.1\pm 7.0\ ppb\ h^{-1}$), which resulted in the accumulation of O_3
421 (the MDA8h O_3 : 85 ppbv) on 22 Sep. When the influence of typhoon disappeared, the direction of airflow
422 turned from northerly into southwest with humid and warm at 500hPa (Fig. S5d), the surface wind on
423 Sep. 23 was affected by the control of the cold northerly airflow (Fig. S5ef). Meteorological conditions
424 including continental high pressure during 23 to 27 Sep. were favorable to the accumulation of air
425 pollutants (Fig. 12). The isoline of 5880 gpm moved from north to the Yangtze River (Fig. 12a,b),
426 indicating the subtropical high pressure was significantly strengthened during 23-27 Sep. 2019. As a result,
427 meteorological conditions such as high temperature, low RH, strong solar radiation, and weak wind speed
428 were conducive to the formation and accumulation of O_3 . The transport rate of O_3 export ($5.4\pm 3.4\ ppb\ h^{-1}$)
429 h^{-1}) on 24-26 Sep. was lower than that on other days ($6.3\pm 4.0\ ppb\ h^{-1}$). Hence, under the combined effects
430 of stable atmospheric conditions and strengthened WPSH, the MDA8h O_3 exceeded the standard of 75
431 ppbv during 24-26 Sep. Previous studies had found that severe multi-day O_3 pollution appeared under the
432 WPSH control (Wang et al., 2018a). Overall, the results indicate that local photochemical production and
433 synoptic situations caused high O_3 concentrations, and regional transport aggravated the O_3 pollution
434 process.

435



436

437 **Figure 12. Synoptic situations of continental high pressure from 20 to 29 Sep. 2019. The gradient color area**
438 **indicates the WPSH over the map and the contour line was from the characteristic isoline of 5880 gpm to the**
439 **center isoline of 5920 gpm. The blue square is the study site.**



440

441 **4 Conclusions**

442 In the present study, we analyzed a typical high O₃ event during 20-29 Sep. 2019 in a coastal city of
443 Southeast China. We clarified the characteristics of AOC, OH reactivity, and radical chemistry, as well as
444 O₃ formation mechanisms using the OBM-MCM model. The predominant oxidant for AOC during the
445 daytime and nighttime was the OH and NO₃, respectively. During the period of O₃ pollution process,
446 OVOCs, NO₂, and CO consumed OH most. Meanwhile, the photolysis of HONO, O₃, HCHO, and other
447 OVOCs were the most important primary sources of RO_x, which played the initiation roles in atmospheric
448 oxidation processes. The radical termination reactions were governed by cross-reactions between RO_x
449 and NO_x. The RIRs and EKMA results showed that the O₃ formation in autumn in coastal city was VOCs-
450 sensitive, and the VOCs were the limited factor of radical recycling and O₃ formation. The reduced
451 emissions of aromatics, alkenes, and long-chain alkanes were benefit for ozone pollution control. The
452 local photochemical production and synoptic situations caused the high concentrations of O₃, and the
453 regional transport aggravated the pollution of ozone. Overall, the results clarified the O₃ pollution process
454 with relatively low local precursor emissions, and implied the fact that O₃ pollution control in coastal
455 cities needs to be further studied.

456

457

458 **Authorship Contribution Statement**

459 Taotao Liu and Youwei Hong contributed equally to this work. Jinsheng Chen and Likun Xue
460 designed and revised the manuscript. Taotao Liu collected the data, contributed to the data analysis.
461 Taotao Liu and Youwei Hong performed chemical modeling analyses of OBM-MCM and wrote the paper.
462 Jinsheng Chen supported funding of observation and research. Lingling Xu, Mengren Li, Chen Yang,
463 Yangbin Dan, Yingnan Zhang, and Min Zhao contributed to discussions of results. Zhi Huang and Hong
464 Wang provided meteorological conditions in Xiamen.

465

466 **Acknowledgment**

467 This study was funded by the Cultivating Project of Strategic Priority Research Program of Chinese
468 Academy of Sciences (XDPB1903), the FJIRSM&IUE Joint Research Fund (RHZX-2019-006), the
469 Center for Excellence in Regional Atmospheric Environment, CAS (E0L1B20201), the Xiamen Youth
470 Innovation Fund Project (3502Z20206094), the foreign cooperation project of Fujian Province
471 (2020I0038) and Xiamen Atmospheric Environment Observation and Research Station of Fujian Province.



472

473 **Reference:**

- 474 Acker, K., Möller, D., Wieprecht, W., Auel, R., Kalaß, D., and Tschervenka, W.: Nitrous and nitric acid
475 measurements inside and outside of clouds at Mt. Brocken, *Water Air Soil Pollut.*, 130, 331–336, 2001.
- 476 Chang, L., Xu, J., Tie, X., and Gao, W.: The impact of Climate Change on the Western Pacific Subtropical High
477 and the related ozone pollution in Shanghai, China, *Sci Rep*, 9, 16998, 10.1038/s41598-019-53103-7, 2019.
- 478 Chen, T., Xue, L., Zheng, P., Zhang, Y., Liu, Y., Sun, J., Han, G., Li, H., Zhang, X., Li, Y., Li, H., Dong, C., Xu, F.,
479 Zhang, Q., and Wang, W.: Volatile organic compounds and ozone air pollution in an oil production region in
480 northern China, *Atmos. Chem. Phys.*, 20, 7069–7086, 10.5194/acp-20-7069-2020, 2020.
- 481 Edwards, P. M., Brown, S. S., Roberts, J. M., Ahmadov, R., Banta, R. M., Degouw, J. A., Dubé, W. P., Field, R. A.,
482 Flynn, J. H., Gilman, J. B., and Graus, M.: High winter ozone pollution from carbonyl photolysis in an oil and gas
483 basin, *Nature*, 514, 351, <https://doi.org/10.1038/nature13767>, 2014.
- 484 Edwards, P. M., Young, C. J., Aikin, K., deGouw, J., Dubé, W. P., Geiger, F., Gilman, J., Helmig, D., Holloway, J.
485 S., Kercher, J., Lerner, B., Martin, R., McLaren, R., Parrish, D. D., Peischl, J., Roberts, J. M., Ryerson, T. B.,
486 Thornton, J., Warneke, C., Williams, E. J., and Brown, S. S.: Ozone photochemistry in an oil and natural gas
487 extraction region during winter: simulations of a snow-free season in the Uintah Basin, Utah, *Atmos. Chem. Phys.*,
488 13, 8955–8971, <https://doi.org/10.5194/acp13-8955-2013>, 2013.
- 489 Eisele, F. L., Mount, G. H., Tanner, D., Jefferson, A., Shetter, R., Harder, J. W., and Williams, E. J.: Understanding
490 the production and interconversion of the hydroxyl radical during the Tropospheric OH Photochemistry Experiment,
491 *J. Geophys. Res.*, 102, 6457–6465, 1997.
- 492 Elshorbany, Y. F., Kurtenbach, R., Wiesen, P., Lissi, E., Rubio, M., Villena, G., Gramsch, E., Rickard, A. R., Pilling,
493 M. J., and Kleffmann, J.: Oxidation capacity of the city air of Santiago, Chile, *Atmos. Chem. Phys.*, 9, 2257–2273,
494 <https://doi.org/10.5194/acp-9-2257-2009>, 2009.
- 495 Emmerson, K. M., Carslaw, N., and Pilling, M. J.: Urban Atmospheric Chemistry During the PUMA Campaign 2:
496 Radical Budgets for OH, HO₂ and RO₂, *J. Atmos. Chem.*, 52, 165–183, 10.1007/s10874-005-1323-2, 2005.
- 497 Fowler, D., Pilegaard, K., Sutton, M. A., Ambus, P., Raivonen, M., Duyzer, J., Simpson, D., Fagerli, H., Fuzzi, S.,
498 Schjoerring, J. K., Granier, C., Neftel, A., Isaksen, I. S. A., Laj, P., Maione, M., Monks, P. S., Burkhardt, J.,
499 Daemmgen, U., Neiryneck, J., Personne, E., Wichink-Kruit, R., Butterbach-Bahl, K., Flechard, C., Tuovinen, J. P.,
500 Coyle, M., Gerosa, G., Loubet, B., Altimir, N., Gruenhage, L., Ammann, C., Cieslik, S., Paoletti, E., Mikkelsen, T.
501 N., Ro-Poulsen, H., Cellier, P., Cape, J. N., Horváth, L., Loreto, F., Niinemets, Ü., Palmer, P. I., Rinne, J., Misztal,
502 P., Nemitz, E., Nilsson, D., Pryor, S., Gallagher, M. W., Vesala, T., Skiba, U., Brüggemann, N., Zechmeister-
503 Boltenstern, S., Williams, J., O'Dowd, C., Facchini, M. C., de Leeuw, G., Flossman, A., Chaumerliac, N., and
504 Erisman, J. W.: Atmospheric composition change: Ecosystems–Atmosphere interactions, *Atmos. Environ.*, 43,
505 5193–5267, 10.1016/j.atmosenv.2009.07.068, 2009.
- 506 George, L. A., Hard, T. M., and O'Brien, R. J.: Measurement of free radicals OH and HO₂ in Los Angeles smog, *J.*
507 *Geophys. Res.*, 104, 11643–11655, 1999.
- 508 Geyer, A., Alicke, B., Konrad, S., Schmitz, T., Stutz, J., and Platt, U.: Chemistry and oxidation capacity of the
509 nitrate radical in the continental boundary layer near Berlin, *J. Geophys. Res.*, 106, 8013–8025,
510 10.1029/2000jd900681, 2001.
- 511 Gong, C., and Liao, H.: A typical weather pattern for the ozone pollution events in North China, *Atmos. Chem.*



- 512 Phys., 10.5194/acp-2019-263, 2019.
- 513 Hofzumahaus, A., Rohrer, F., Lu, K. D., Bohn, B., Brauers, T., Chang, C. C., Fuchs, H., Holland, F., Kita, K.,
514 Kondo, Y., Li, X., Lou, S. R., Shao, M., Zeng, L. M., Wahner, A., and Zhang, Y. H.: Amplified Trace Gas Removal
515 in the Troposphere, *Science*, 324, 1702–1704, 2009.
- 516 Hong, Z., MengzeLi, HongWang, LinglingXu, Hong, Y., Chen, J., Chen, J., Zhang, H., Zhang, Y., Wu, X., Hu, B.,
517 and Li, M.: Characteristics of atmospheric volatile organic compounds (VOCs) at a mountainous forest site and
518 two urban sites in the southeast of China, *Sci Total Environ*, 10.1016/j.scitotenv.2018.12.132, 2019.
- 519 Hu B, Liu T, Yang Y, Hong Y, Li M, Xu L, Wang H, Chen N, Wu X, Chen J: Characteristics and Formation
520 Mechanism of Surface Ozone in a Coastal Island of Southeast China: Influence of Sea-land Breezes and Regional
521 Transport. *Aerosol Air Qual. Res.*, 19(8):1734-1748, 2019.
- 522 Hu, B., Duan, J., Hong, Y., Xu, L., Li, M., Bian, Y., Qin, M., Fang, W., Xie, P., and Chen, J.: Exploration of the
523 atmospheric chemistry of nitrous acid in a coastal city of southeastern China: Results from measurements across
524 four seasons, *Atmos. Chem. Phys. Discuss.* [preprint], <https://doi.org/10.5194/acp-2020-880>, 2020a.
- 525 Hu, B., Liu, T., Hong, Y., Xu, L., Li, M., Wu, X., Wang, H., Chen, J., and Chen, J.: Characteristics of peroxyacetyl
526 nitrate (PAN) in a coastal city of southeastern China: Photochemical mechanism and pollution process, *Sci Total
527 Environ*, 719, 137493, 10.1016/j.scitotenv.2020.137493, 2020b.
- 528 Jenkin, M. E., Saunders, S. M., Wagner, V., and Pilling, M. J.: Protocol for the development of the Master Chemical
529 Mechanism, MCM v3 (Part B): tropospheric degradation of aromatic volatile organic compounds, *Atmos. Chem.
530 Phys.*, 3, 181–193, <https://doi.org/10.5194/acp-3-181-2003>, 2003.
- 531 Jiang Y, Xue L, Gu R, Jia M, Zhang Y, Wen L, Zheng P, Chen T, Li H, Shan Y et al: Sources of nitrous acid (HONO)
532 in the upper boundary layer and lower free troposphere of the North China Plain: insights from the Mount Tai
533 Observatory. *Atmos. Chem. Phys.*, 20(20):12115-12131, 2020.
- 534 Kanaya, Y., Cao, R. Q., Akimoto, H., Fukuda, M., Komazaki, Y., Yokouchi, Y., Koike, M., Tanimoto, H., Takegawa,
535 N., and Kondo, Y.: Urban photochemistry in central Tokyo: 1. Observed and modeled OH and HO₂ radical
536 concentrations during the winter and summer of 2004, *J. Geophys. Res.*, 112, D21312, doi:10.1029/2007JD008670,
537 2007.
- 538 Kanaya, Y., Matsumoto, J., Kato, S., and Akimoto, H.: Behavior of OH and HO₂ radicals during the Observations
539 at a Remote Island of Okinawa (ORION99) field campaign 2. Comparison between observations and calculations,
540 *J. Geophys. Res.*, 106, 24209–24223, 2001.
- 541 Kovacs, T. A., Brune, W. H., Harder, H., Martinez, M., Simpasa, J. B., Frost, G. J., Williams, E., Jobson, T., Stroud,
542 C., Young, V., Fried, A., and Wert, B.: Direct measurements of urban OH reactivity during Nashville SOS in
543 summer 1999, *J. of Environ. Monitor.*, 5, 68-74, 10.1039/b204339d, 2003.
- 544 Li, B., Ho, S. S. H., Gong, S., Ni, J., Li, H., Han, L., Yang, Y., Qi, Y., and Zhao, D.: Characterization of VOCs and
545 their related atmospheric processes in a central Chinese city during severe ozone pollution periods, *Atmos. Chem.
546 Phys.*, 19, 617-638, 10.5194/acp-19-617-2019, 2019.
- 547 Li, N., He, Q., Greenberg, J., Guenther, A., Cao, J., & Wang, J., Liao H., Zhang Q.: Impacts of biogenic and
548 anthropogenic emissions on summertime ozone formation in the Guanzhong Basin, China, *Atmos. Chem. Phys.*,
549 2018a.
- 550 Li, Z., Xue, L., Yang, X., Zha, Q., Tham, Y. J., Yan, C., Louie, P. K. K., Luk, C. W. Y., Wang, T., and Wang, W.:
551 Oxidizing capacity of the rural atmosphere in Hong Kong, Southern China, *Sci Total Environ*, 612, 1114-1122,
552 10.1016/j.scitotenv.2017.08.310, 2018.



- 553 Lin, H., Wang, M., Duan, Y., Fu, Q., Ji, W., Cui, H., Jin, D., Lin, Y., and Hu, K.: O₃ Sensitivity and Contributions
554 of Different NMHC Sources in O₃ Formation at Urban and Suburban Sites in Shanghai, *Atmosphere*, 11, 295,
555 10.3390/atmos 11030295, 2020.
- 556 Ling, Z., Zhao, J., Fan, S., and Wang, X.: Sources of formaldehyde and their contributions to photochemical O₃
557 formation at an urban site in the Pearl River Delta, southern China, *Chemosphere*, 168, 1293-1301,
558 10.1016/j.chemosphere. 2016.11.140, 2017.
- 559 Liu, J., Wang, L., Li, M., Liao, Z., Sun, Y., Song, T., Gao, W., Wang, Y., Li, Y., Ji, D., Hu, B., Kerminen, V.-M.,
560 Wang, Y., and Kulmala, M.: Quantifying the impact of synoptic circulation patterns on ozone variability in northern
561 China from April to October 2013Ó2017, *Atmos. Chem. Phys.*, 19, 14477-14492, 10.5194/acp-19-
562 14477-2019, 2019a.
- 563 Liu, T., Hu, B., Xu, X., Hong, Y., Zhang, Y., Wu, X., Xu, L., Li, M., Chen, Y., Chen, X., and Chen, J.: Characteristics
564 of PM_{2.5}-bound secondary organic aerosol tracers in a coastal city in Southeastern China: Seasonal patterns and
565 pollution identification, *Atmos. Environ.*, 237, 117710, 10.1016/j.atmosenv. 2020.117710, 2020a.
- 566 Liu, T., Hu, B., Yang, Y., Li, M., Hong, Y., Xu, X., Xu, L., Chen, N., Chen, Y., Xiao, H., and Chen, J.: Characteristics
567 and source apportionment of PM_{2.5} on an island in Southeast China: Impact of sea-salt and monsoon, *Atmos. Res.*,
568 235, 104786, 10.1016/j.atmosres.2019.104786, 2020b.
- 569 Liu, X., Lyu, X., Wang, Y., Jiang, F., and Guo, H.: Intercomparison of O₃ formation and radical chemistry in the
570 past decade at a suburban site in Hong Kong, *Atmos. Chem. Phys.*, 19, 5127-5145, 10.5194/acp-19-5127-2019,
571 2019b.
- 572 Liu, X., Wang, N., Lyu, X., Zeren, Y., Jiang, F., Wang, X., Zou, S., Ling, Z., and Guo, H.: Photochemistry of ozone
573 pollution in autumn in Pearl River Estuary, South China, *Sci Total Environ*, 754, 141812,
574 10.1016/j.scitotenv.2020.141812, 2020c.
- 575 Liu, Z., Wang, Y., Gu, D., Zhao, C., Huey, L., Stickel, R., Liao, J., Shao, M., Zhu, T., Zeng, L., Amoroso, A.,
576 Costabile, F., Chang, C., and Liu, S.: Summertime photochemistry during CARE Beijing-2007:
577 ROß budgets and Oß formation, *Atmos. Chem. Phys.*, 12, 7737-
578 7752, 10.5194/acp-12-7737-2012, 2012.
- 579 Lou, S., Holland, F., Rohrer, F., Lu, K., Bohn, B., Brauers, T., Chang, C. C., Fuchs, H., Haeseler, R., Kita, K.,
580 Kondo, Y., Li, X., Shao, M., Zeng, L., Wahner, A., Zhang, Y., Wang, W., and Hofzumahaus, A.: Atmospheric OH
581 reactivities in the Pearl River Delta - China in summer 2006: measurement and model results, *Atmos. Chem. Phys.*,
582 10, 11243-11260, 10.5194/acp-10-11243-2010, 2010a.
- 583 Lou, S., Holland, F., Rohrer, F., Lu, K., Bohn, B., Brauers, T., Chang, C., Fuchs, H., Häeseler, R., Kita, K., Kondo,
584 Y., Li, X., Shao, M., Zeng, L., Wahner, A., Zhang, Y., Wang, W., and Hofzumahaus, A.: Atmospheric OH reactivities
585 in the Pearl River Delta – China in summer 2006: measurement and model results, *Atmos. Chem. Phys.*, 10, 11243-
586 11260, 10.5194/acp-10-11243-2010, 2010b.
- 587 Lu, X., Hong, J., Zhang, L., Copper, O. R., Schultz, M. G., Xu, X., Wang, T., Gao, M., Zhao, Y., Zhang, Y. Severe
588 Surface Ozone Pollution in China: A Global Perspective. *Environ. Sci. Technol. Lett.*, 5, 487-494, 2018.
- 589 Mao, J., Ren, X., Chen, S., Brune, W. H., Chen, Z., Martinez, M., Harder, H., Lefer, B., Rappenglück, B., Flynn,
590 J., and Leuchner, M.: Atmospheric oxidation capacity in the summer of Houston 2006: Comparison with summer
591 measurements in other metropolitan studies, *Atmos. Environ.*, 44, 4107-4115, 10.1016/j.atmosenv.2009.01.013,
592 2010.
- 593 Martinez, M.: OH and HO₂ concentrations, sources, and loss rates during the Southern Oxidants Study in Nashville,



- 594 Tennessee, summer 1999, *J. Geophys. Res.*, 108, 10.1029/2003jd003551, 2003.
- 595 Mazzuca, G. M., Ren, X., Loughner, C.P., Estes, M., Crawford, J. H., Pickering, K. E., Weinheimer, A. J., Dickerson,
596 R. R.: Ozone production and its sensitivity to NO_x and VOCs: results from the DISCOVER-AQ field experiment,
597 Houston 2013. *Atmos. Chem. Phys.* 16, 14463–14474, 2016.
- 598 Michoud, V., Kukui, A., Camredon, M., Colomb, A., Borbon, A., Miet, K., Aumont, B., Beekmann, M., Durand-
599 Jolibois, R., Perrier, S., Zapf, P., Siour, G., Ait-Helal, W., Locoge, N., Sauvage, S., Afif, C., Gros, V., Furger, M.,
600 Ancellet, G., and Doussin, J. F.: Radical budget analysis in a suburban European site during the MEGAPOLI
601 summer field campaign, *Atmos. Chem. Phys.*, 12, 11951–11974, 10.5194/acp-12-11951-2012, 2012.
- 602 Ren, X., Brune, W. H., Cantrell, C. A., Edwards, G. D., Shirley, T., Metcalf, A. R., and Leshner, R. L.: Hydroxyl and
603 peroxy radical chemistry in a rural area of Central Pennsylvania: Observations and model comparisons, *J. Atmos.*
604 *Chem.*, 52, 231–257, 10.1007/s10874-005-3651-7, 2005.
- 605 Rollins, A. W., Browne, E. C., Min, K. E., Pusede, S. E., Wooldridge, P. J., Gentner, D. R., Goldstein, A. H., Liu,
606 S., Day, D. A., Russell, L. M., and Cohen, R. C.: Evidence for NO_x Control over Nighttime SOA Formation,
607 *Science*, 337, 1210–1212, 2012.
- 608 Saunders, S. M., Jenkin, M. E., Derwent, R. G., and Pilling, M. J.: Protocol for the development of the Master
609 Chemical Mechanism, MCM v3 (Part A): tropospheric degradation of nonaromatic volatile organic compounds,
610 *Atmos. Chem. Phys.*, 3, 161–180, doi:10.5194/acp-3-161-2003, 2003.
- 611 Sheehy, P. M., Volkamer, R., Molina, L. T., and Molina, M. J.: Oxidative capacity of the Mexico City atmosphere
612 – Part 2: A RO₂ radical cycling perspective, *Atmos. Chem. Phys.*, 10, 6993–7008,
613 10.5194/acp-10-6993-2010, 2010.
- 614 Simon, H., Reff, A., Wells, B., Xing, J., and Frank, N.: Ozone trends across the United States over a period of
615 decreasing NO_x and VOC emissions, *Environ. Sci. Technol.*, 49, 186–195, 10.1021/es504514z, 2015.
- 616 Smith, S. C., Lee, J. D., Bloss, W. J., Johnson, G. P., Ingham, T., and Heard, D. E.: Concentrations of OH and HO₂
617 radicals during NAMBLEX: measurements and steady state analysis, *Atmos. Chem. Phys.*, 6, 1435–1453,
618 doi:10.5194/acp-6-1435-2006, 2006.
- 619 Tan, Z., Lu, K., Jiang, M., Su, R., Dong, H., Zeng, L., Xie, S., Tan, Q., and Zhang, Y.: Exploring ozone pollution
620 in Chengdu, southwestern China: A case study from radical chemistry to O₃-VOC-NO_x sensitivity, *Sci Total*
621 *Environ.* 636, 775–786, 10.1016/j.scitotenv.2018.04.286, 2018.
- 622 Tan, Z., Lu, K., Jiang, M., Su, R., Wang, H., Lou, S., Fu, Q., Zhai, C., Tan, Q., Yue, D., Chen, D., Wang, Z., Xie,
623 S., Zeng, L., and Zhang, Y.: Daytime atmospheric oxidation capacity in four Chinese megacities during the
624 photochemically polluted season: a case study based on box model simulation, *Atmos. Chem. Phys.*, 19, 3493–
625 3513, 10.5194/acp-19-3493-2019, 2019.
- 626 Volkamer, R., Sheehy, P., Molina, L. T., and Molina, M. J.: Oxidative capacity of the Mexico City atmosphere –
627 Part 1: A radical source perspective, *Atmos. Chem. Phys.*, 10, 6969–6991, 10.5194/acp-10-6969-2010, 2010.
- 628 Wang, H., Lyu, X., Guo, H., Wang, Y., Zou, S., Ling, Z., Wang, X., Jiang, F., Zeren, Y., Pan, W., Huang, X., and
629 Shen, J.: Ozone pollution around a coastal region of South China Sea: interaction between marine and continental
630 air, *Atmos. Chem. Phys.*, 18, 4277–4295, 10.5194/acp-18-4277-2018, 2018a.
- 631 Wang, H., Tan, S., Wang, Y., Jiang, C., Shi, G., Zhang, M., Che, H.: A multisource observation study of the severe
632 prolonged regional haze episode over eastern China in January 2013. *Atmos. Environ.* 89, 807–815, 2014.
- 633 Wang, M., Chen, W., Zhang, L., Qin, W., Zhang, Y., Zhang, X., and Xie, X.: Ozone pollution characteristics and



- 634 sensitivity analysis using an observation-based model in Nanjing, Yangtze River Delta Region of China, *J Environ*
635 *Sci (China)*, 93, 13-22, 10.1016/j.jes.2020.02.027, 2020.
- 636 Wang, Y., Guo, H., Zou, S., Lyu, X., Ling, Z., Cheng, H., and Zeren, Y.: Surface O₃ photochemistry over the South
637 China Sea: Application of a near-explicit chemical mechanism box model, *Environ Pollut*, 234, 155-166,
638 10.1016/j.envpol.2017.11.001, 2018b.
- 639 Whalley, L. K., Stone, D., Bandy, B., Dunmore, R., Hamilton, J. F., Hopkins, J., Lee, J. D., Lewis, A. C., and Heard,
640 D. E.: Atmospheric OH reactivity in central London: observations, model predictions and estimates of in situ ozone
641 production, *Atmos. Chem. Phys.*, 16, 2109-2122, 10.5194/acp-16-2109-2016, 2016.
- 642 Wu, X., Li, M., Chen, J., Wang, H., Xu, L., Hong, Y., Zhao, G., Hu, B., Zhang, Y., Dan, Y., and Yu, S.: The
643 characteristics of air pollution induced by the quasi-stationary front: Formation processes and influencing factors,
644 *Sci Total Environ*, 707, 136194, 10.1016/j.scitotenv.2019.136194, 2020.
- 645 Wu, X., Xu, L., Hong, Y., Chen, J., Qiu, Y., Hu, B., Hong, Z., Zhang, Y., Liu, T., Chen, Y., Bian, Y., Zhao, G., Chen,
646 J., and Li, M.: The air pollution governed by subtropical high in a coastal city in Southeast China: Formation
647 processes and influencing mechanisms, *Sci Total Environ*, 692, 1135-1145, 10.1016/j.scitotenv.2019.07.341, 2019.
- 648 Xue, L. K., Wang, T., Gao, J., Ding, A. J., Zhou, X. H., Blake, D. R., Wang, X. F., Saunders, S. M., Fan, S. J., Zuo,
649 H. C., Zhang, Q. Z., and Wang, W. X.: Ground-level ozone in four Chinese cities: precursors, regional transport
650 and heterogeneous processes, *Atmos. Chem. Phys.*, 14, 13175-13188, 10.5194/acp-14-13175-2014, 2014.
- 651 Xue, L., Gu, R., Wang, T., Wang, X., Saunders, S., Blake, D., Louie, P. K. K., Luk, C. W. Y., Simpson, I., Xu, Z.,
652 Wang, Z., Gao, Y., Lee, S., Mellouki, A., and Wang, W.: Oxidative capacity and radical chemistry in the polluted
653 atmosphere of Hong Kong and Pearl River Delta region: analysis of a severe photochemical smog episode, *Atmos.*
654 *Chem. Phys.*, 16, 9891-9903, 10.5194/acp-16-9891-2016, 2016.
- 655 Zeren, Y., Guo, H., Lyu, X., Jiang, F., Wang, Y., Liu, X., Zeng, L., Li, M., and Li, L.: An Ozone “Pool” in South
656 China: Investigations on Atmospheric Dynamics and Photochemical Processes Over the Pearl River Estuary, *J.*
657 *Geophys. Res.*, 124, 12340-12355, 10.1029/2019jd030833, 2019.
- 658 Zhang L , Brook J R , Vet R . A revised parameterization for gaseous dry deposition in air-quality models. *Atmos.*
659 *Chem. Phys.*, 3(2), 2067-2082, 2003.
- 660 Zhang, Y., Hong, Z., Chen, J., Xu, L., Hong, Y., Li, M., Hao, H., Chen, Y., Qiu, Y., Wu, X., Li, J.-R., Tong, L., and
661 Xiao, H.: Impact of control measures and typhoon weather on characteristics and formation of PM_{2.5} during the
662 2016 G20 summit in China, *Atmos. Environ.*, 224, 117312, 10.1016/j.atmosenv.2020.117312, 2020a.
- 663 Zhang, Y., Xu, L., Zhuang, M., Zhao, G., Chen, Y., Tong, L., Yang, C., Xiao, H., Chen, J., Wu, X., Hong, Y., Li,
664 M., Bian, Y., and Chen, Y.: Chemical composition and sources of submicron aerosol in a coastal city of China:
665 Results from the 2017 BRICS summit study, *Sci Total Environ*, 741, 140470, 10.1016/j.scitotenv.2020.140470,
666 2020b.
- 667 Zhang, Y. , Xue, L. , Carter, W. , Pei, C. , and Wang, W.: Development of Ozone Reactivity Scales for Volatile
668 Organic Compounds in a Chinese Megacity, *Atmos. Chem. Phys.*, 10.5194/acp-2021-44, 2021
- 669 Zhu, J., Wang, S., Wang, H., Jing, S., Lou, S., Saiz-Lopez, A., and Zhou, B.: Observationally constrained modeling
670 of atmospheric oxidation capacity and photochemical reactivity in Shanghai, China, *Atmos. Chem. Phys.*, 20, 1217-
671 1232, 10.5194/acp-20-1217-2020, 2020.

672